Supplement of Atmos. Chem. Phys., 26, 4089–4104, 2026
https://doi.org/10.5194/acp-26-4089-2026-supplement
© Author(s) 2026. CC BY 4.0 License.

Atmospheric Chemistry and Physics
Open Access
EGU

Supplement of

Spatiotemporal patterns of temperature inversions and impacts on surface $PM_{2.5}$ across China

Yonglin Fang et al.

Correspondence to: Hancheng Hu (dame712@outlook.com)

The copyright of individual parts of the supplement might differ from the article licence.

This supplementary material includes 23 Figs, 4 Tables.

Fig S1. Site filtering method. (a) Relationship between distance and the number of matching stations. (b) Example diagram of site matching process. 'r' represents the distance from the nearest air quality monitoring station to the sounding station.

Fig S2. Distribution of all radiosonde stations and air monitoring stations in China as of 2021. The inset map in the lower right shows the South China Sea Islands.

Table S1. Metadata of the 75 radiosonde stations used in this study (Including altitude changes due to site relocation)

Fig S3. Example diagram of original radio sounding profile, taking Beijing Station at BJT 08:00 on Nov 7,2017 as an example.

Fig S4. (a) The fine-scale distribution of SBI base heights at 10-m intervals (0-100 m); (b) The full vertical distribution of EI base heights at 100-m intervals (100-2000 m).

Fig S5. Inversion frequency of TI, SBI and EI at BJT 08:00.

Fig S6. Inversion frequency of TI, SBI and EI at BJT 20:00.

S1. Characterizing the seasonal evolution of TIs by integrating wind speed and humidity datasets.

Fig S7. Seasonal comparison of meteorological conditions within the boundary layer (0–1000 m).

Fig S8. Inversion strength of TI, SBI and EI at BJT 08:00.

Fig S9. Inversion strength of TI, SBI and EI at BJT 20:00.

Fig S10. Inversion thickness of TI, SBI and EI at BJT 08:00.

Fig S11. Inversion thickness of TI, SBI and EI at BJT 20:00.

Table S2. Annual mean values of temperature inversion parameters by region at BJT 08:00.

Table S3. Annual mean values of temperature inversion parameters by region at BJT 20:00.

Fig S12. Distribution of $PM_{2.5}$ concentration differences with and without temperature inversion at BJT 08:00.

Fig S13. Distribution of $PM_{2.5}$ concentration differences with and without temperature inversion at BJT 20:00.

Fig S14. Fitting relationship between inversion thickness and $PM_{2.5}$ concentration across seven regions of China from 2016 to 2021.

Fig S15. Inversion frequency of TI, SBI and EI (dual color axis display).

S2. Discussion on using the temperature difference (ΔT) as an indicator for inversion strength.

Fig S16. Spatial and seasonal distribution of lapse rate for different types of TI.

Fig S17. Fitting relationship between lapse rate and $PM_{2.5}$ concentration across seven regions of China from 2016 to 2021. The ends of the boxes, the ends of the bars, and the short line across each box represent the 25th and 75th percentiles, the 5th and 95th percentiles, and the median, respectively. Each strength interval contains a sample size $\geqslant$ 10.

Table S4. Correlation coefficients between inversion parameters and $PM_{2.5}$ concentrations. '\' indicates insignificance.

Fig S18. Distribution of TI frequency across different thickness thresholds.

Fig S19. Distribution of SBI frequency across different thickness thresholds.

Fig S20. Distribution of EI frequency across different thickness thresholds.

S3. Case studies in BTH, YRD, and PRD.

Fig S21. Temporal variations of temperature inversion (TI) strength and surface $PM_{2.5}$ concentrations during severe pollution episodes in representative cities. (a) Beijing (BTH region), (b) Nanjing (YRD region), and (c) Yangjiang (PRD region). The black line represents TI strength (ΔT, left axis), and the red line represents $PM_{2.5}$ concentration (right axis).

S4. Analysis of the "Inversion-Dispersion" Paradox in South China.

Fig S22. Spatial distribution of the Potential Source Contribution Function (PSCF) values for $PM_{2.5}$ during the study period. The analysis is based on 48-h backward trajectories at an altitude of 500 m. (a) Wuhan (representative of Central China), showing dominant potential sources from the North China Plain. (b) Guangzhou (representative of South China), indicating potential transport pathways primarily from Central China and the eastern coast.

Fig S23. Roses of the mean boundary-layer wind (0–1000 m) in SC. (a) Patterns during non-inversion periods. (b) Patterns during the presence of EIs. Note that EIs are typically associated with stronger northerly winds (ventilation), while non-inversion periods are dominated by weaker southerly winds.

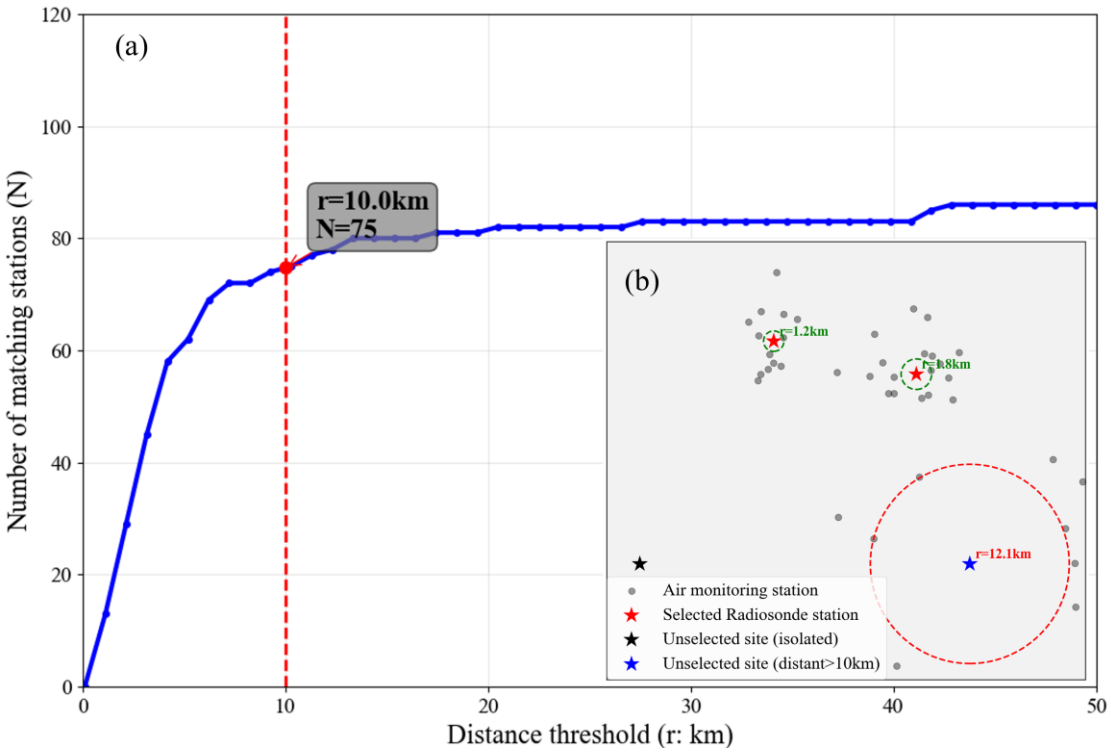

Fig S1. Site filtering method. (a) Relationship between distance and the number of matching stations. (b) Example diagram of site matching process. 'r' represents the distance from the nearest air quality monitoring station to the sounding station. Panel (b) is a schematic illustration of the nearest-neighbor matching method within a defined radius, not a plot of actual station coordinates.

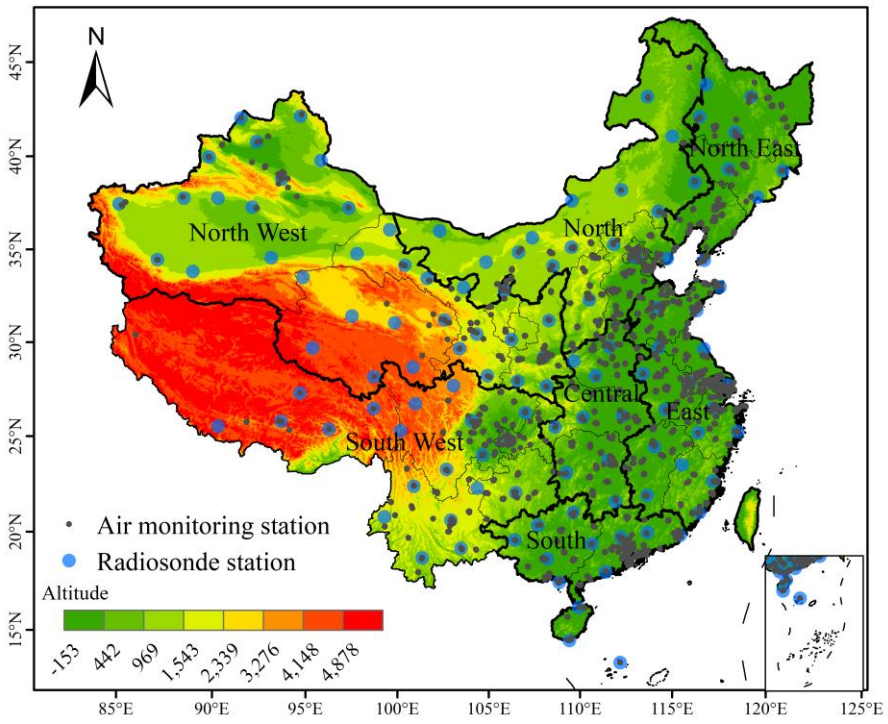

Fig S2. Distribution of all radiosonde stations and air monitoring stations in China as of 2021. The inset map in the lower right shows the South China Sea Islands.

Table S1. Metadata of the 75 radiosonde stations used in this study (Including altitude changes due to site relocation)

Station_Name	Station_ID	Latitude	Longitude	Altitude (m)	Region
Aksu	51628	41.12	80.38	1108	North West
Ankang	57245	32.7166	109.0333	291	North West
Anqing	58424	30.623	116.9672	63	East
Baise	59211	23.9027	106.6063	176	South
Beihai	59644	21.4475	109.1836	14	South
Beijing	54511	39.8061	116.4694	32	North
Qamdo	56137	31.1472	97.175	3305\3313	South West
Chifeng	54218	42.3	118.8333	669	North
Dachuan	57328	31.2075	107.5067	344	South West
Dongsheng	53543	39.8152	110.0122	1463	North
Fuzhou	58847	26.0969	119.2319	85\112	East
Fuyang	58203	32.8966	115.8336	32	East
Ganxian	57993	25.8705	115.0141	139	East
Gejiu	56985	23.4444	103.3278	1315	South West
Guiyang	57816	26.5897	106.7275	1223\1227	South West
Guilin	57957	25.32	110.3	165	South
Harbin	50953	45.9333	126.5667	119	North East
Hami	52203	42.805	93.5172	738	North West
Haikou	59758	19.9941	110.2466	65	South
Hailar	50527	49.25	119.7002	650	North
Hanzhong	57127	33.0677	107.0402	509	North West

Hangzhou	58457	30.2258	120.1647	43	East
Hezuo	56080	34.9911	102.9047	2911	North West
Hetian	51828	37.1205	79.925	1375	North West
Hechi	59023	24.6938	108.0391	261	South
Heyuan	59293	23.8	114.7333	71	South
Hongjia	58665	28.618	121.4163	5	East
Hohhot	53463	40.8558	111.5713	1154	North
Jiuquan	52533	39.7711	98.487	1478	North West
Karamay	51243	45.6108	84.845	451	North West
Kongtong	53915	35.5311	106.66	1348\1469	North West
Kunming	56778	25.0078	102.6531	1888	South West
Lhasa	55591	29.6586	91.1352	3649	South West
Lijiang	56651	26.8469	100.2175	2381	South West
Nyingchi	56312	29.6475	94.3605	2991	South West
Linhe	53513	40.7219	107.3705	1042	North
Nagqu	55299	31.4794	92.0611	4508	South West
Nanchang	58606	28.59	115.9011	48	East
Nanjing	58238	31.9333	118.9	36	East
Nanning	59431	22.78	108.55	113\153	South
Qiqihar	50745	47.3761	123.9236	148	North East
Qingdao	54857	36.0666	120.3333	77	East
Qingyuan	59280	23.7102	113.0847	80	South
Quzhou	58633	28.9938	118.8908	84	East
Rongcheng	54778	37.1463	122.3725	79	East
Shapingba	57516	29.6047	106.4041	542	South West
Xiamen	59134	24.4856	118.0797	141	East
Shantou	59316	23.3847	116.68	4	South
Simao	56964	22.8161	100.9911	1303\1417	South West
Huaihua	57749	27.6069	110.0305	259	Central
Tacheng	51133	46.7325	82.98	536	North West
Tongliao	54135	43.5952	122.2602	182	North
Wenjiang	56187	30.75	103.8667	548	South West
Urumqi	51463	43.7891	87.6452	936	North West
Wuzhou	59265	23.4783	111.3036	116	South
Wudu	56096	33.4025	104.9175	1079	North West
Wuhan	57494	30.6	114.05	23	Central
Xichang	56571	27.9042	102.2672	1559\1592	South West
Xining	52866	36.6625	101.7327	2297\2410	North West
Xilinhot	54102	43.95	116.1197	1005	North
Xuzhou	58027	34.2872	117.158	42	East
Yan'an	53845	36.5758	109.4497	1180	North West
Yanji	54292	42.8741	129.5038	258	North East
Yangjiang	59663	21.8453	111.9784	90	South
Yichun	50774	47.7	128.8333	259\266	North East
Yining	51431	43.9405	81.3263	664	North West
Yibin	56492	28.7689	104.6053	340\503	South West
Yichang	57416	30.7333	111.3667	258	Central

Yinchuan	53614	38.4717	106.2081	1113	North West
Yuzhong	52983	35.8667	104.15	1876	North West
Yushu	56029	33.0013	96.9647	3718\3725	North West
Zhangjiakou	54401	40.7694	114.9194	774	North
Zhangqiu	54727	36.6533	117.5172	123\264	East
Changchun	54161	43.8913	125.2316	238	North East
Zhengzhou	57083	34.7167	113.65	112	Central

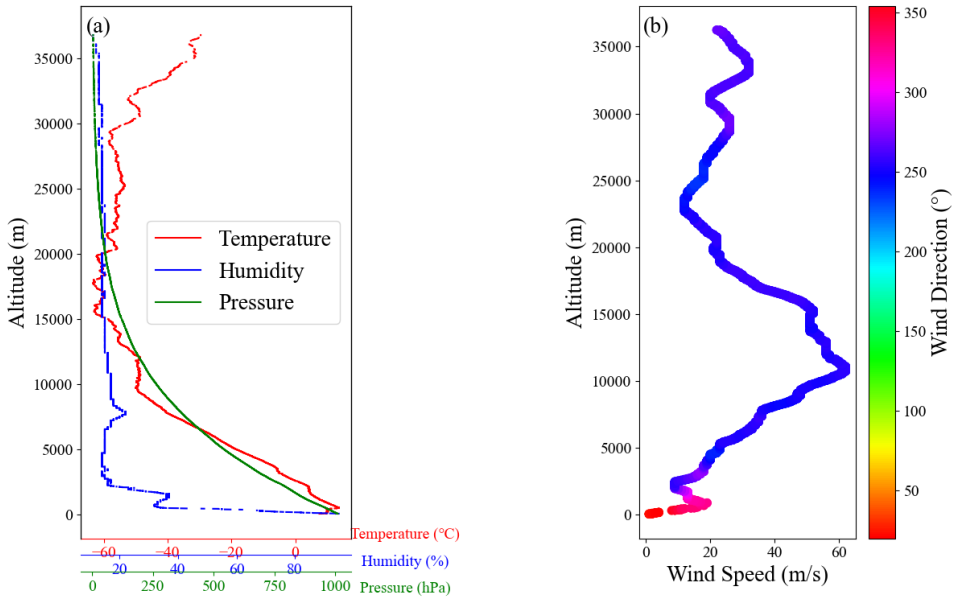

Fig S3. Example diagram of original radio sounding profile, taking Beijing Station at BJT 08:00 on Nov 7,2017 as an example

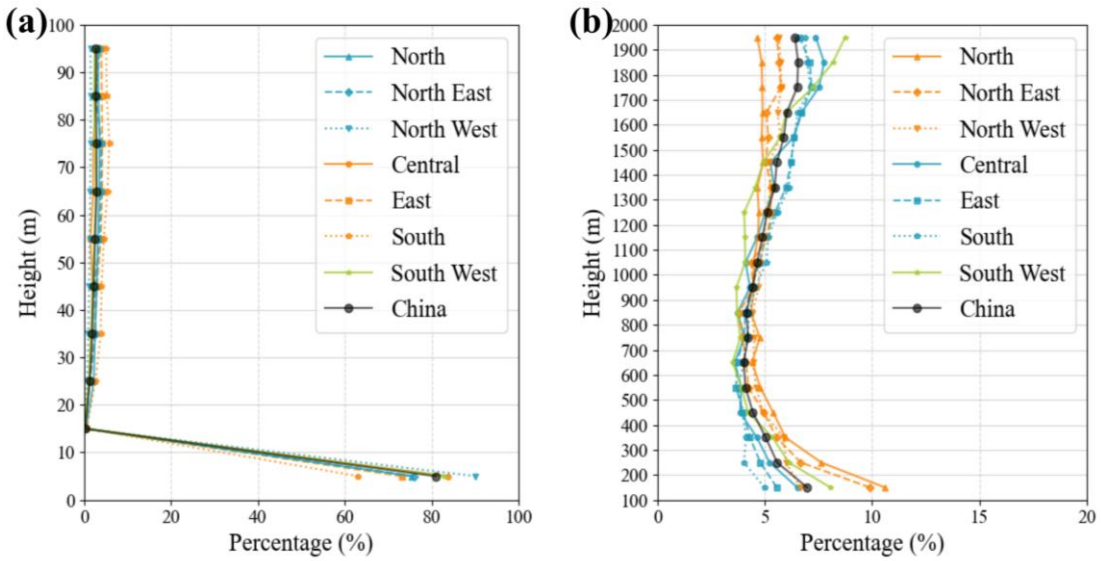

Fig S4. (a) The fine-scale distribution of SBI base heights at 10-m intervals (0-100 m); (b) The full vertical distribution of EI base heights at 100-m intervals (100-2000 m).

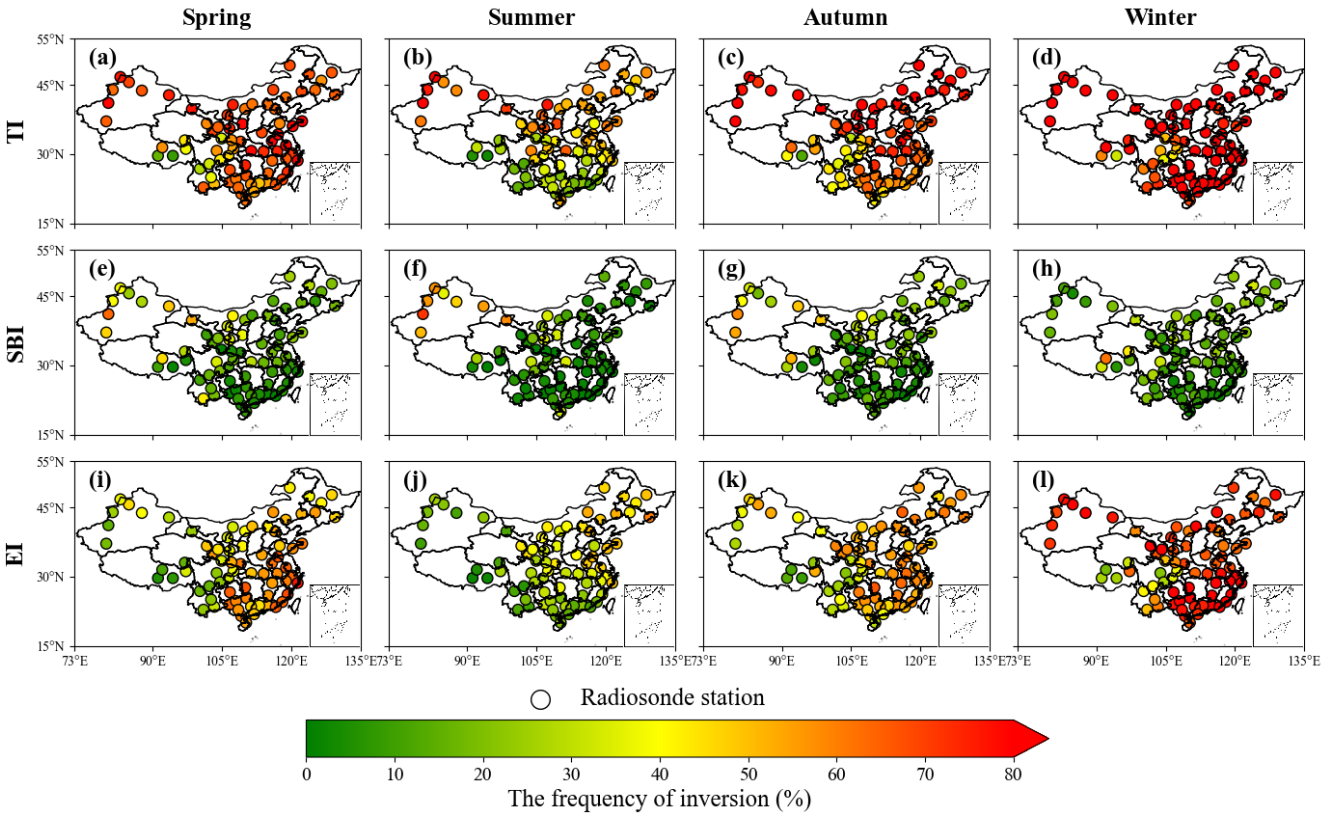

Fig S5. Inversion frequency of TI, SBI and EI at BJT 08:00.

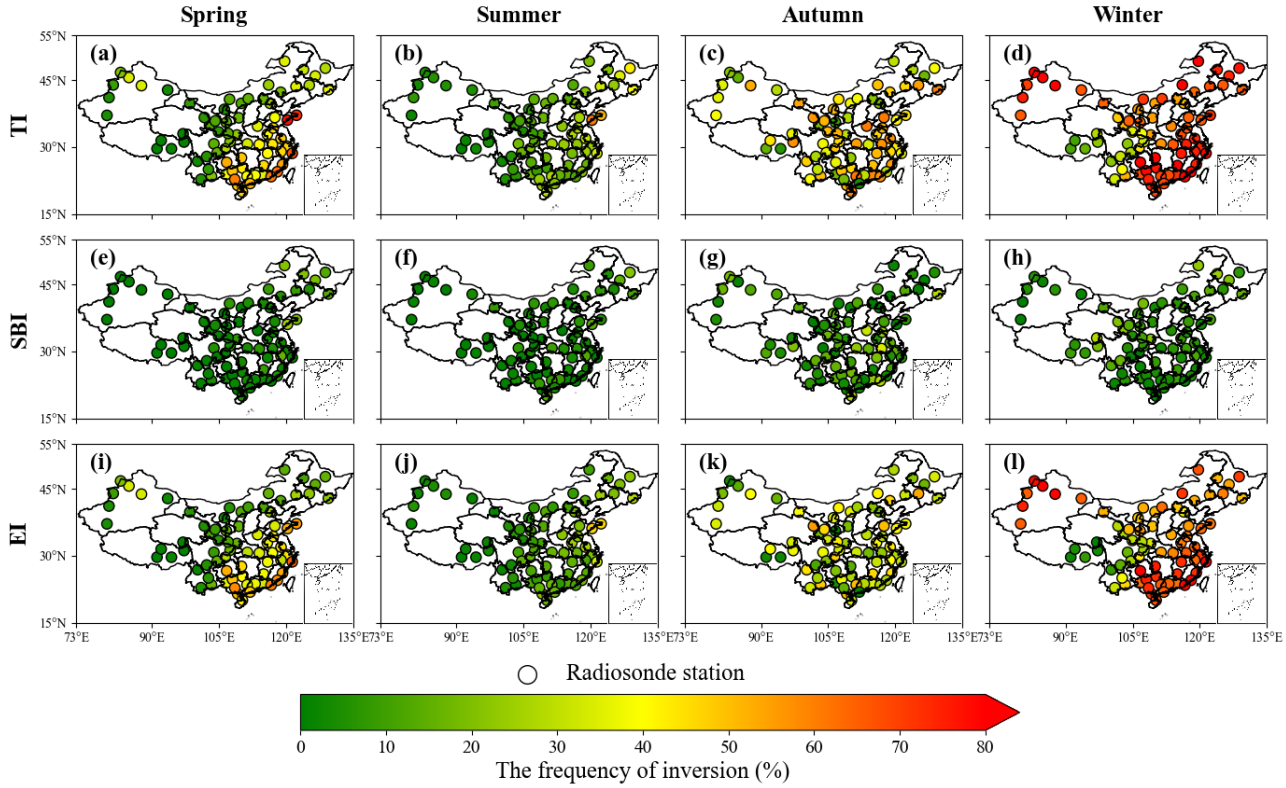

Fig S6. Inversion frequency of TI, SBI and EI at BJT 20:00.

S1. Characterizing the seasonal evolution of TIs by integrating wind speed and humidity datasets.

To quantify the meteorological background, we analyzed the mean wind speed and relative humidity within the 0–1000 m layer. This vertical range was selected as a representative proxy for the lower troposphere, encompassing the primary domain of pollutant dispersion and inversion development while ensuring statistical consistency across seasons (regardless of the fluctuating boundary layer height). The results reveal that the wintertime peak in TI frequency is primarily thermodynamically driven. Interestingly, the mean boundary-layer wind speed is generally higher in winter than in summer across most regions (Fig. S7b), a condition that typically enhances turbulent mixing and disrupts inversion formation. However, this dynamic suppression is overridden by favorable thermodynamic conditions. Winter is characterized by significantly lower relative humidity (e.g., ~56% in NE vs. ~71% in summer; Fig. S7a). This drier atmosphere minimizes downward longwave radiation, which, combined with the extended duration of winter nights, maximizes nocturnal radiative cooling efficiency. Consequently, the strong radiative cooling in winter compensates for the enhanced wind shear, sustaining a high frequency of inversions.

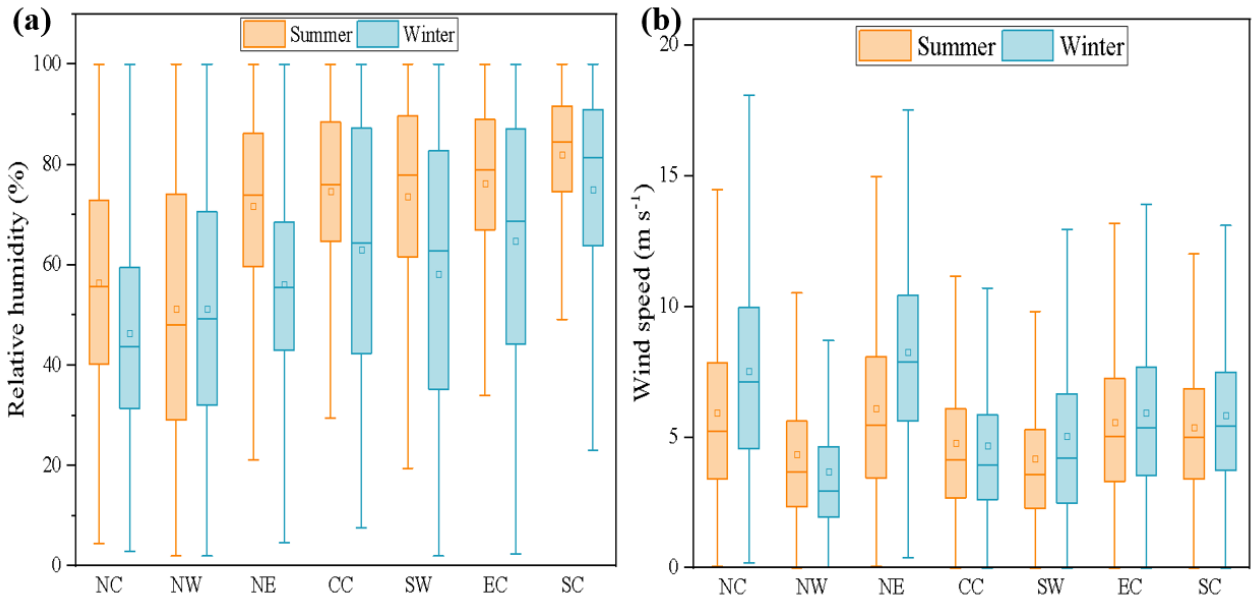

Fig S7. Seasonal comparison of meteorological conditions within the boundary layer (0–1000 m).

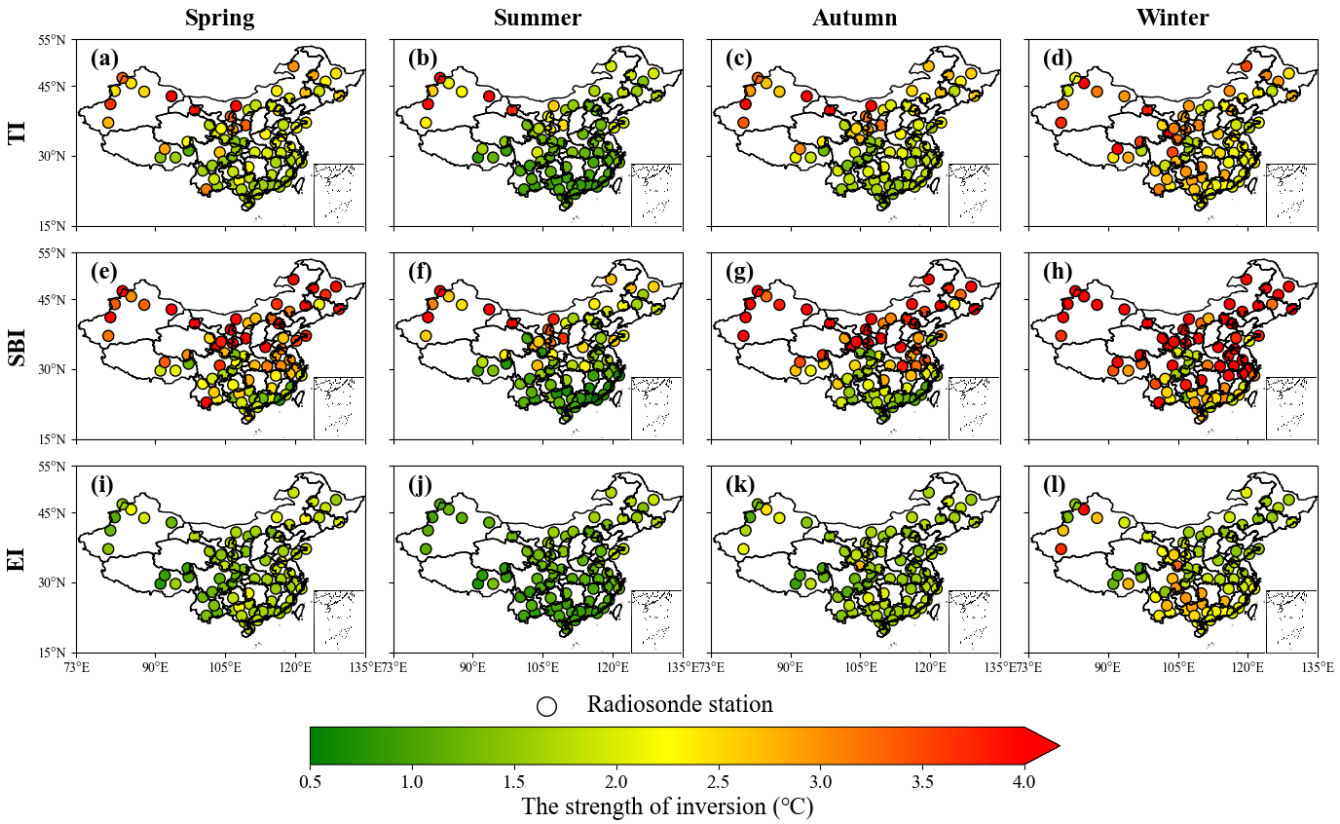

Fig S8. Inversion strength of TI, SBI and EI during at BJT 08:00.

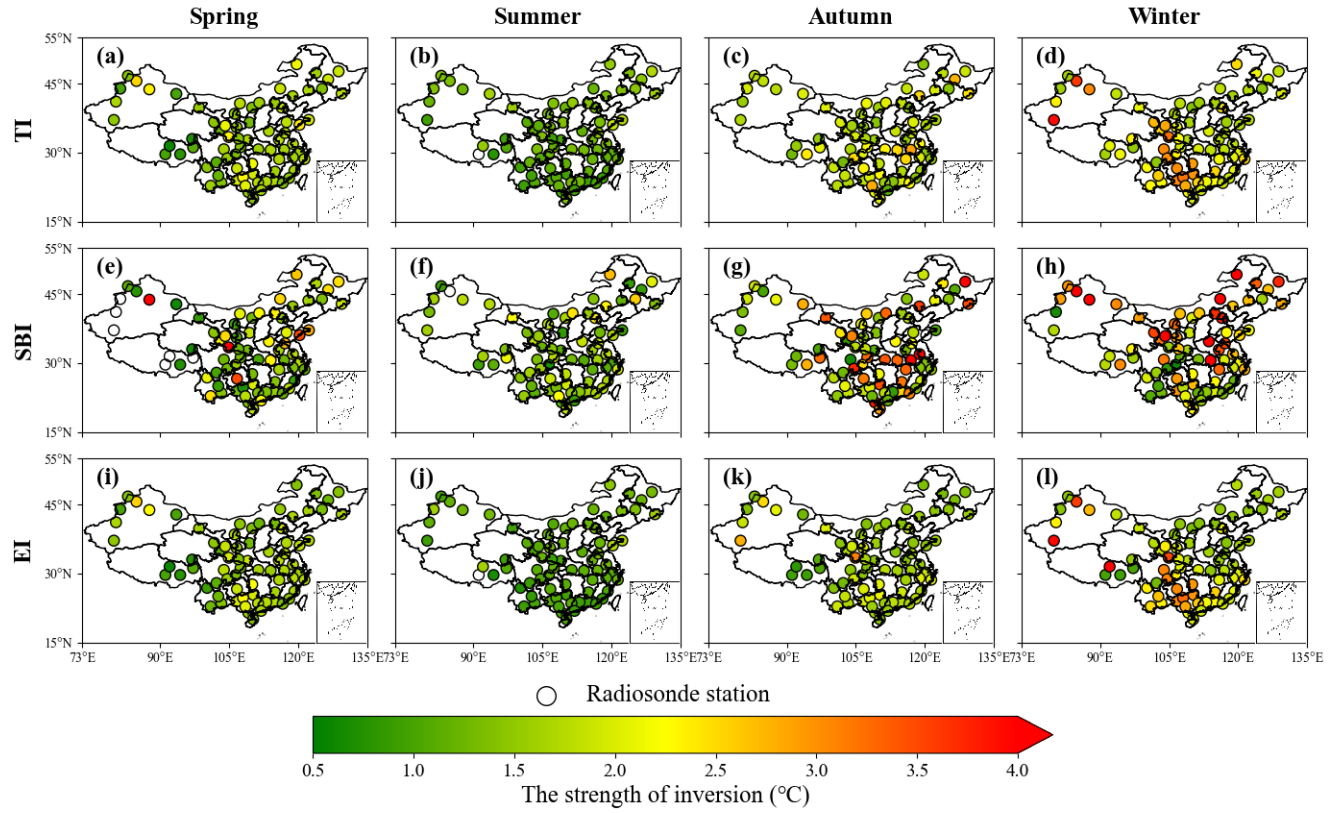

Fig S9. Inversion strength of TI, SBI and EI during at BJT 20:00.

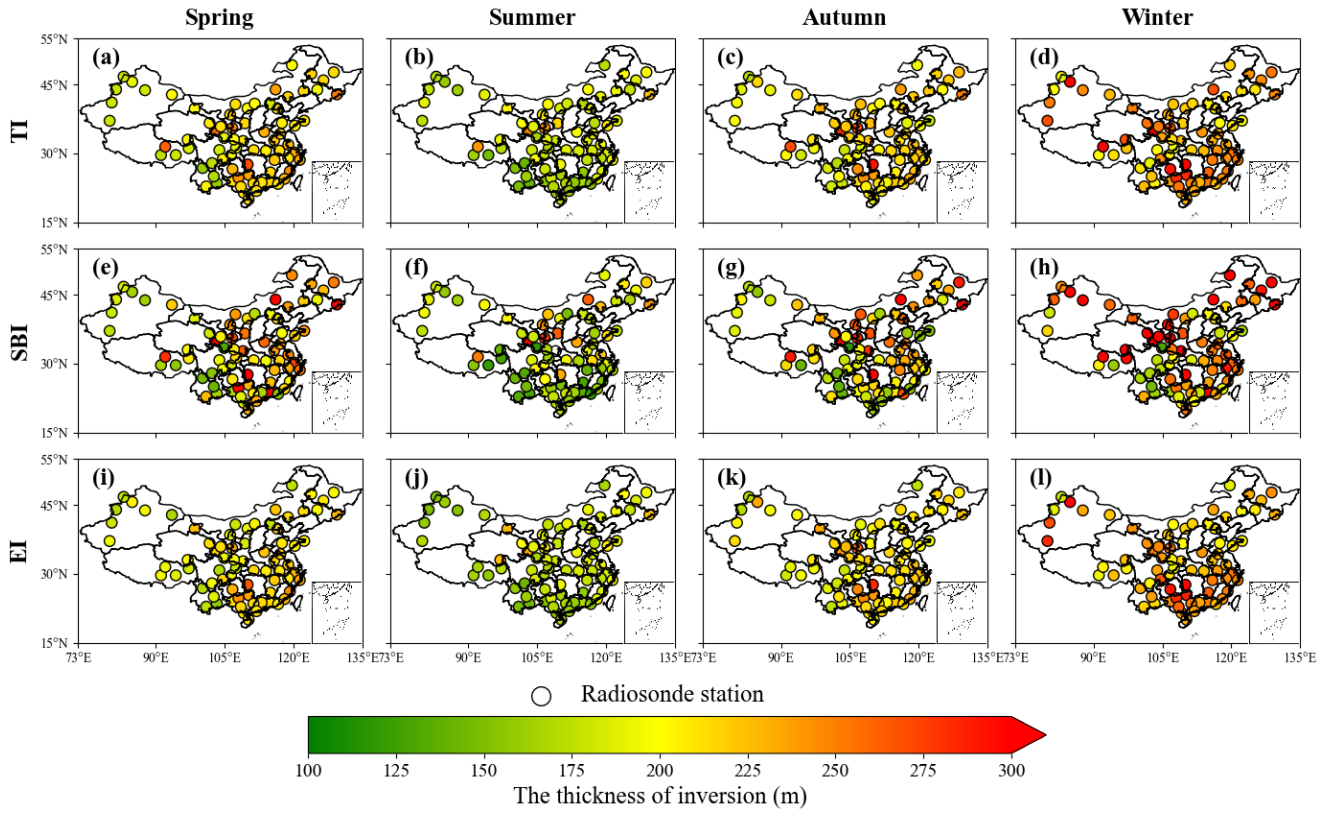

Fig S10. Inversion thickness of TI, SBI and EI during at BJT 08:00.

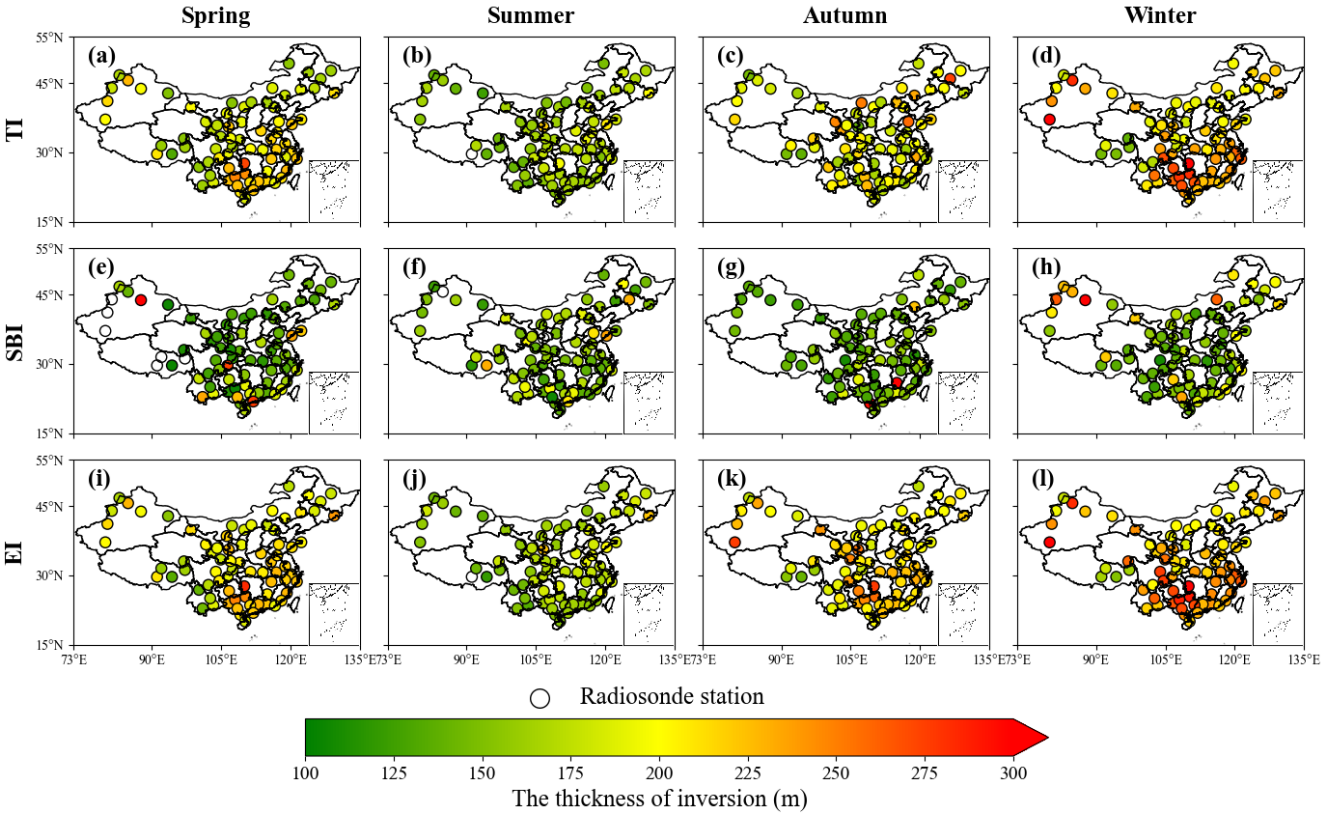

Fig S11. Inversion thickness of TI, SBI and EI during at BJT 20:00.

Table S2. Annual mean values of temperature inversion parameters by region at BJT 08:00.

Region	TI			SBI			EI		
	F_{TI}(%)	ΔT(℃)	ΔH(m)	F_{SBI}(%)	ΔT(℃)	ΔH(m)	F_{EI}(%)	ΔT(℃)	ΔH(m)
Central	70.0	2.16	233	14.5	3.91	249	55.0	1.76	233
East	67.0	1.92	219	9.2	2.84	221	57.8	1.74	219
North	72.6	2.36	210	18.6	4.30	237	54.0	1.68	200
North East	70.7	2.32	223	16.1	4.26	258	54.6	1.71	213
North West	70.5	2.81	219	26.0	4.19	235	44.5	1.86	216
South	56.5	1.87	222	6.1	1.78	204	50.4	1.87	225
South West	43.7	2.07	204	15.0	2.55	196	28.7	1.61	201

Table S3. Annual mean values of temperature inversion parameters by region at BJT 20:00.

Region	TI			SBI			EI		
	F_{TI}(%)	ΔT(℃)	ΔH(m)	F_{SBI}(%)	ΔT(℃)	ΔH(m)	F_{EI}(%)	ΔT(℃)	ΔH(m)
Central	44.4	1.95	228	5.5	2.80	149	38.9	1.85	239
East	51.5	1.79	213	6.3	2.10	161	45.2	1.75	220
North	38.9	1.90	184	11.1	2.80	152	27.8	1.52	196
North East	48.1	1.80	195	15.9	2.39	162	32.2	1.48	210
North West	28.7	2.21	206	5.4	2.88	174	23.3	1.99	218
South	44.6	1.99	224	3.8	1.67	166	40.8	2.02	230
South West	18.9	1.84	186	4.2	1.67	156	14.7	1.76	198

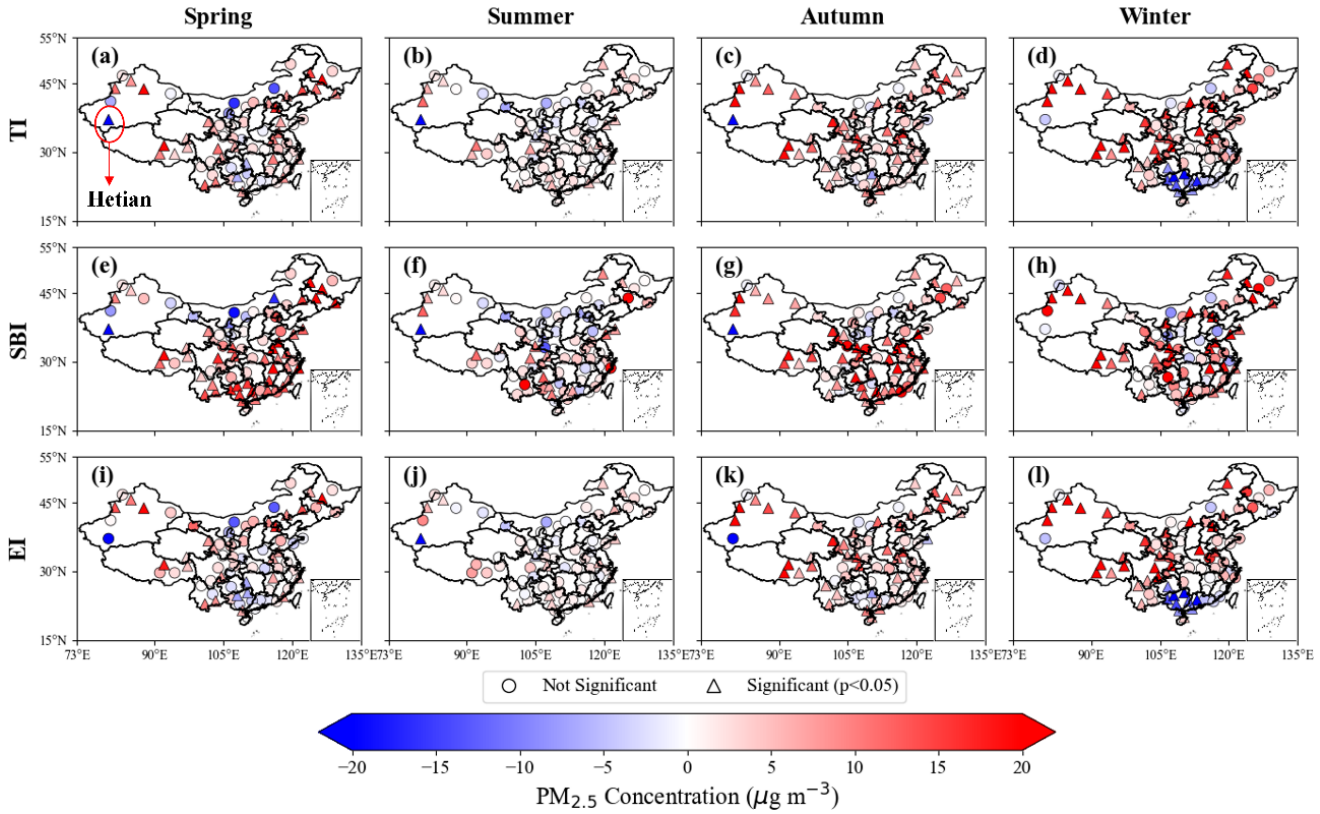

Fig S12. Distribution of $PM_{2.5}$ concentration differences with and without temperature inversion at BJT 08:00.

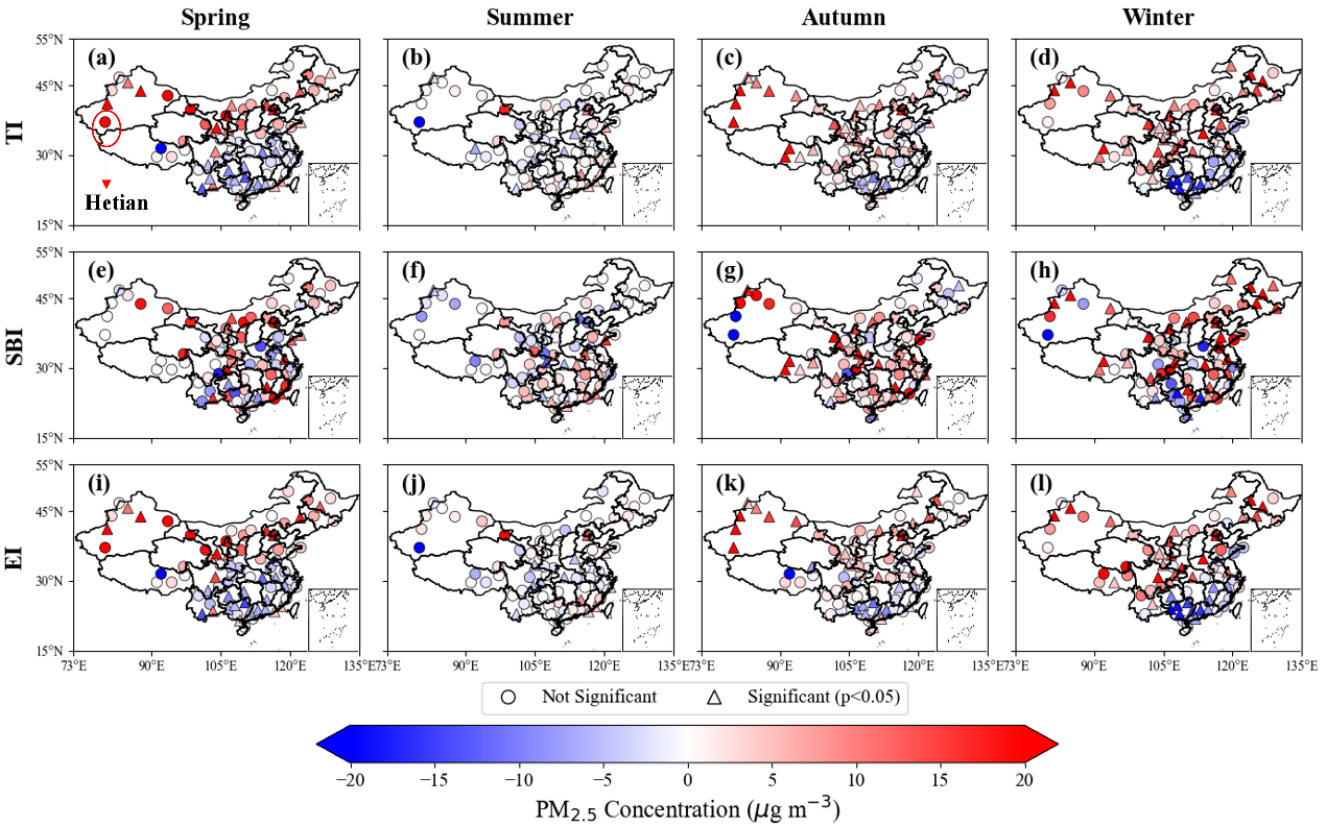

Fig S13. Distribution of $PM_{2.5}$ concentration differences with and without temperature inversion at BJT 20:00.

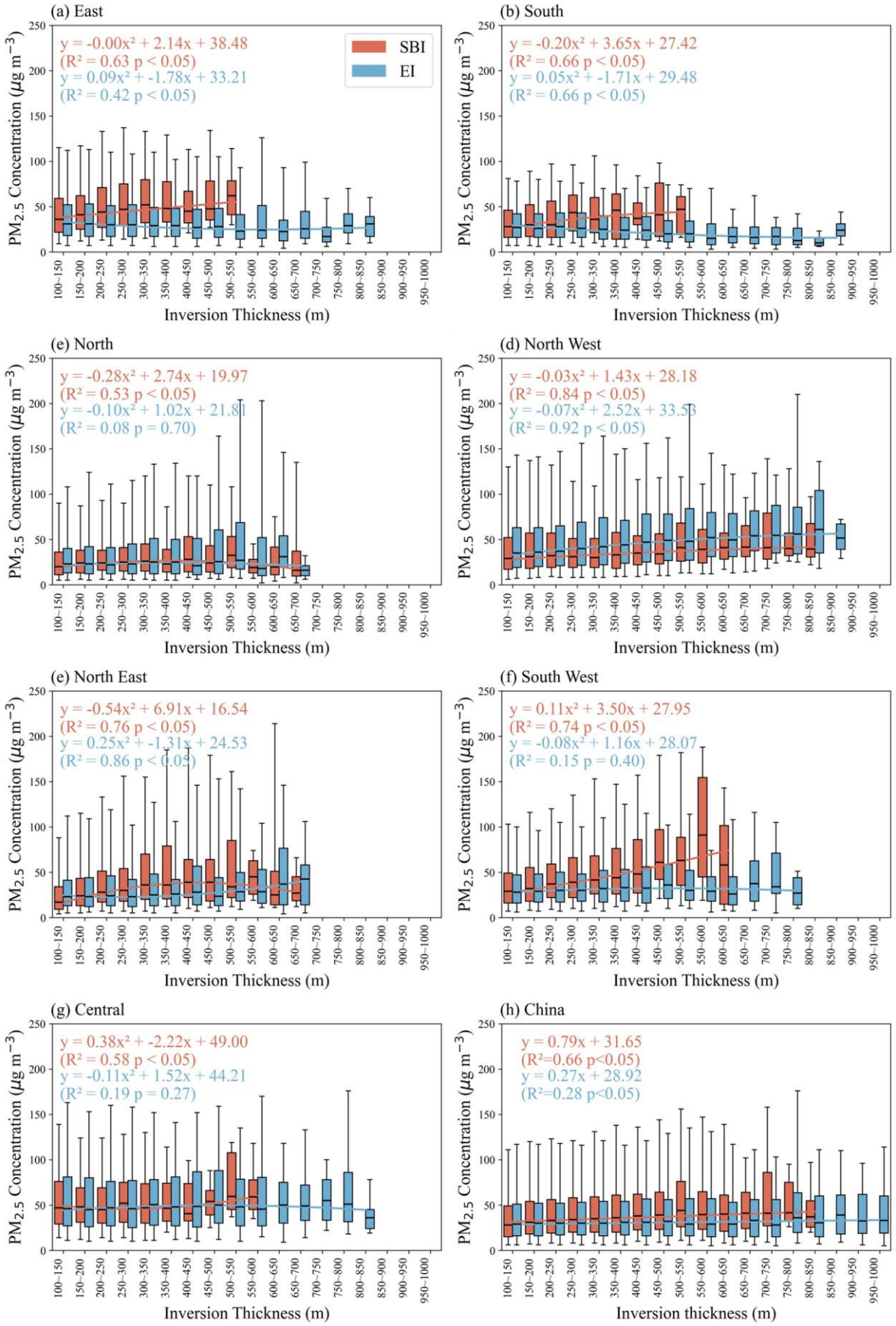

Fig S14. Fitting relationship between inversion thickness and $PM_{2.5}$ concentration across seven regions of China from 2016 to 2021. The ends of the boxes, the ends of the bars, and the short line across each box represent the 25th and 75th percentiles, the 5th and 95th percentiles, and the median, respectively. Each strength interval contains a sample size ≥ 10.

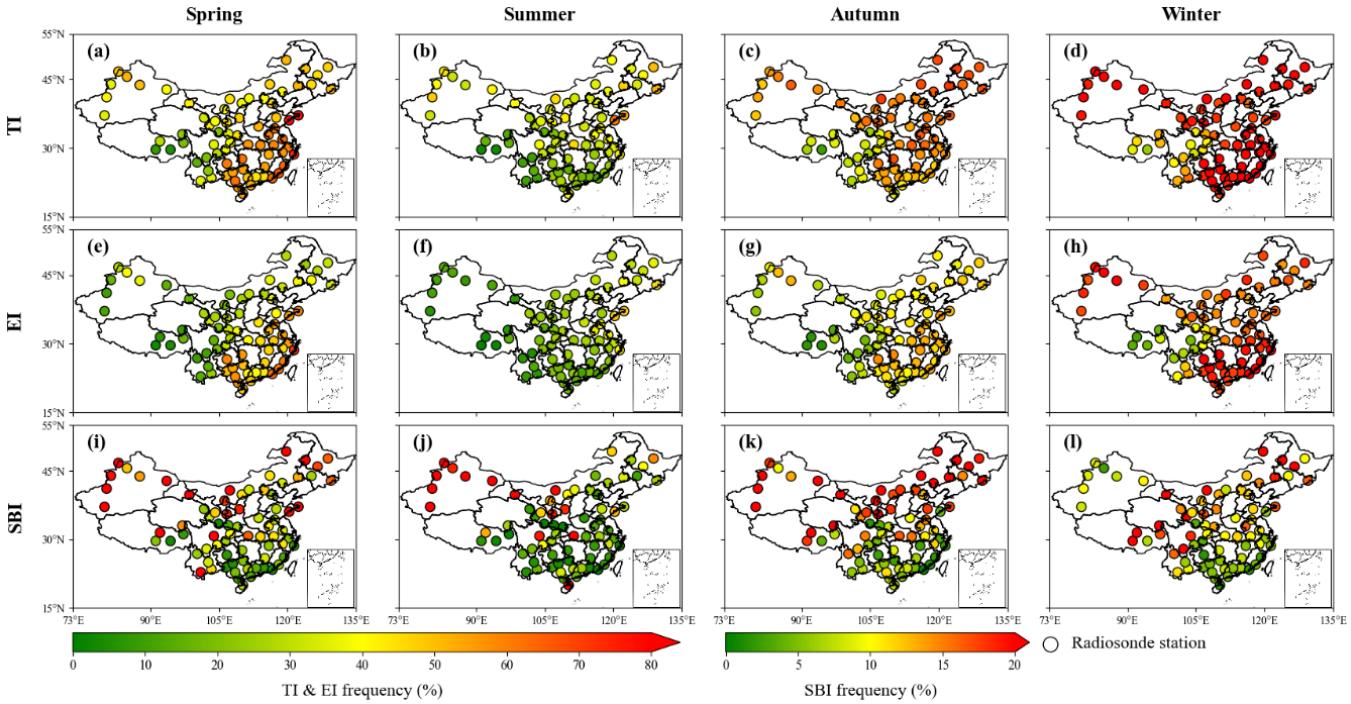

Fig S15. Inversion frequency of TI, SBI and EI (dual color axis display).

S2. Discussion on using the temperature difference (ΔT) as an indicator for inversion strength.

To determine the most effective metric for characterizing the impact of inversions on air quality, we compared the correlations of $PM_{2.5}$ with ΔT, TI thickness, and temperature lapse rate (ΔT/ΔH). The statistical analysis reveals that ΔT exhibits the highest correlation with $PM_{2.5}$, followed by thickness, while the lapse rate shows the weakest correlation (Table S4.). This suggests that for pollution accumulation, the total 'energy barrier' (represented by ΔT) is a more critical factor than the local stability gradient (lapse rate). Although a high lapse rate implies strong local stability, such layers—if thin—can be rapidly eroded by surface heating. In contrast, a large ΔT typically implies a significant heat deficit that persists longer, effectively suppressing vertical mixing and trapping pollutants. Based on these empirical findings, we retained TI strength as the primary indicator in this study.

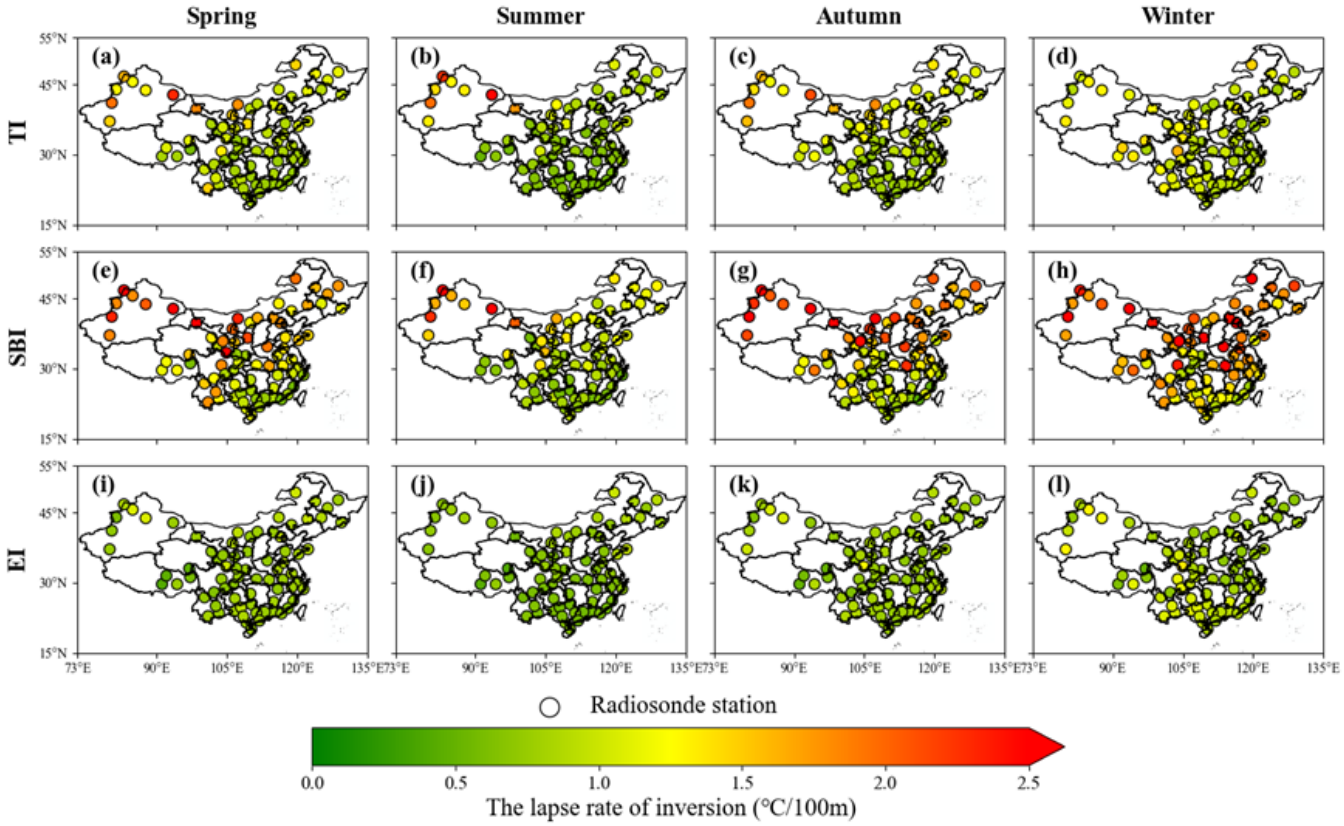

Fig S16. Spatial and seasonal distribution of lapse rate for different types of TI.

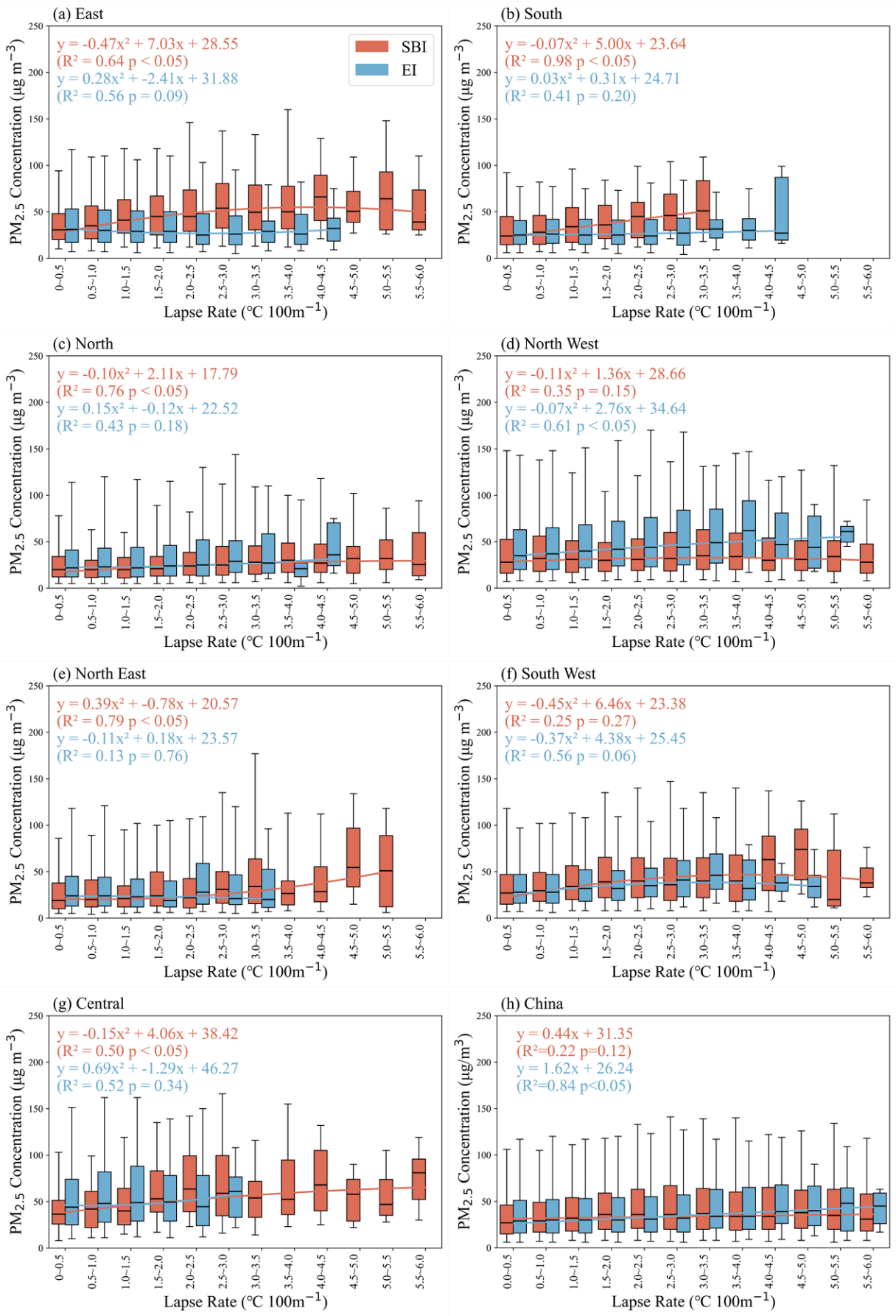

Fig S17. Fitting relationship between lapse rate and $PM_{2.5}$ concentration across seven regions of China from 2016 to 2021. The ends of the boxes, the ends of the bars, and the short line across each box represent the 25th and 75th percentiles, the 5th and 95th percentiles, and the median, respectively. Each strength interval contains a sample size ≥ 10.

Table S4. Correlation coefficients between inversion parameters and $PM_{2.5}$ concentrations. '\' indicates insignificance.

Region/R^2	Inversion Strength		Inversion Thickness		Lapse Rate	
	SBI	EI	SBI	EI	SBI	EI
East	0.98	0.82	0.63	0.42	0.64	\
South	0.97	0,92	0.66	0.66	0.98	\
North	0.90	0.78	0.53	\	0.76	\
North West	0.47	0.78	0.84	0.92	\	0.61
North East	0.83	\	0.76	0.86	0.79	\
South West	0.94	0.66	0.74	\	\	\
Central	\	\	0.58	\	0.50	\
China	0.72	0.66	0.66	0.28	\	0.84

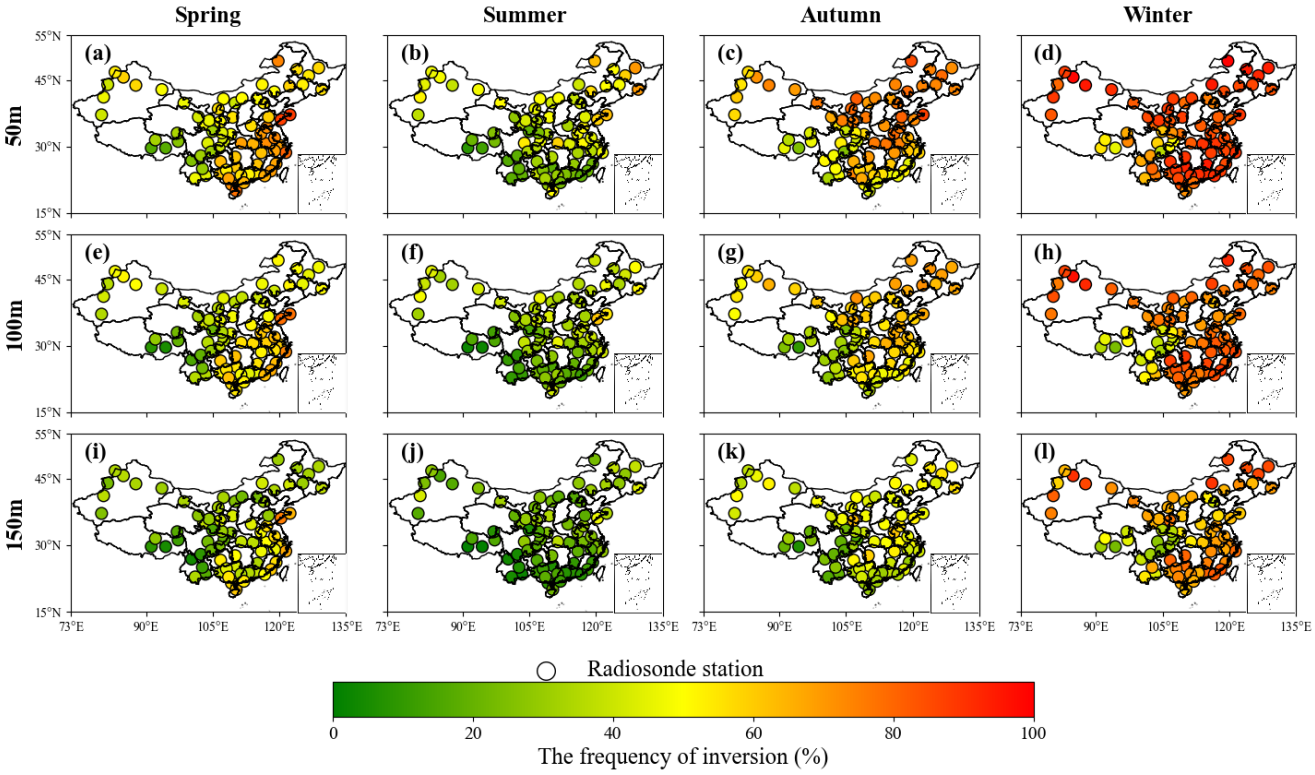

Fig S18. Distribution of TI frequency across different thickness thresholds.

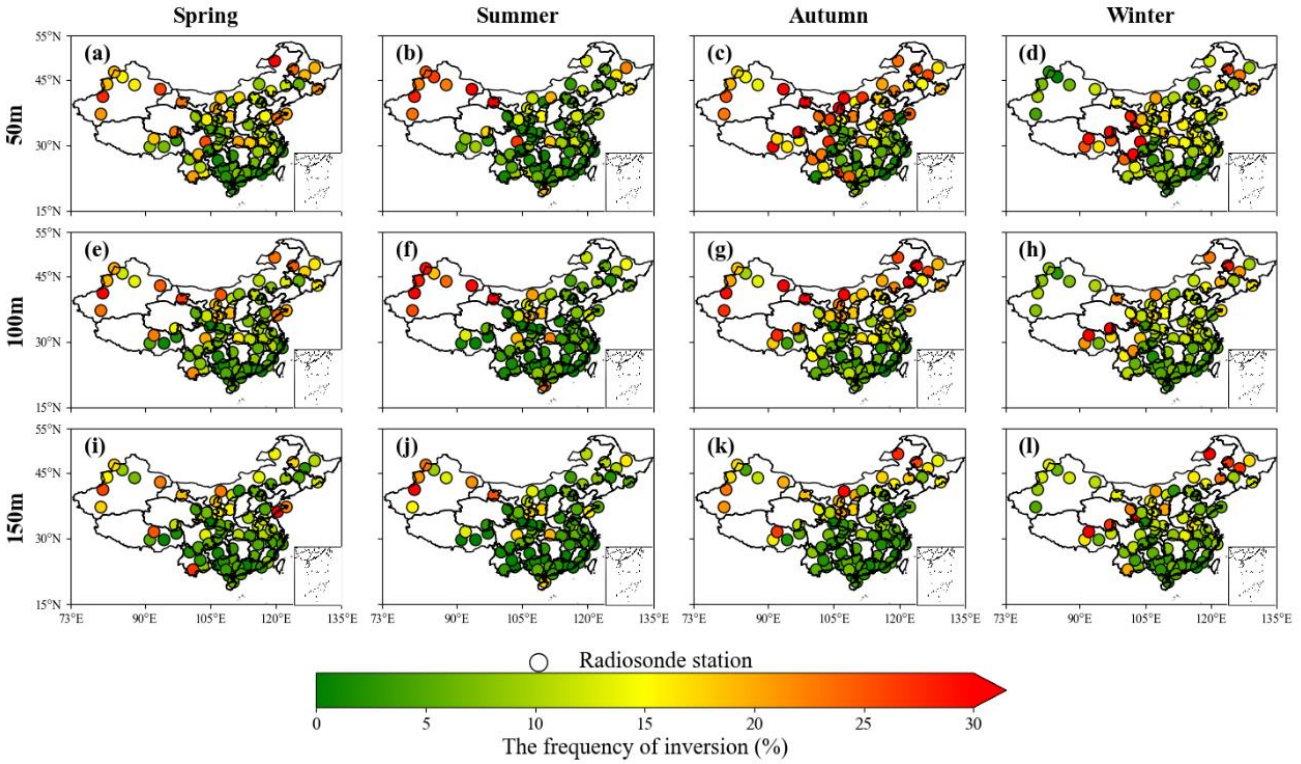

Fig S19. Distribution of SBI frequency across different thickness thresholds.

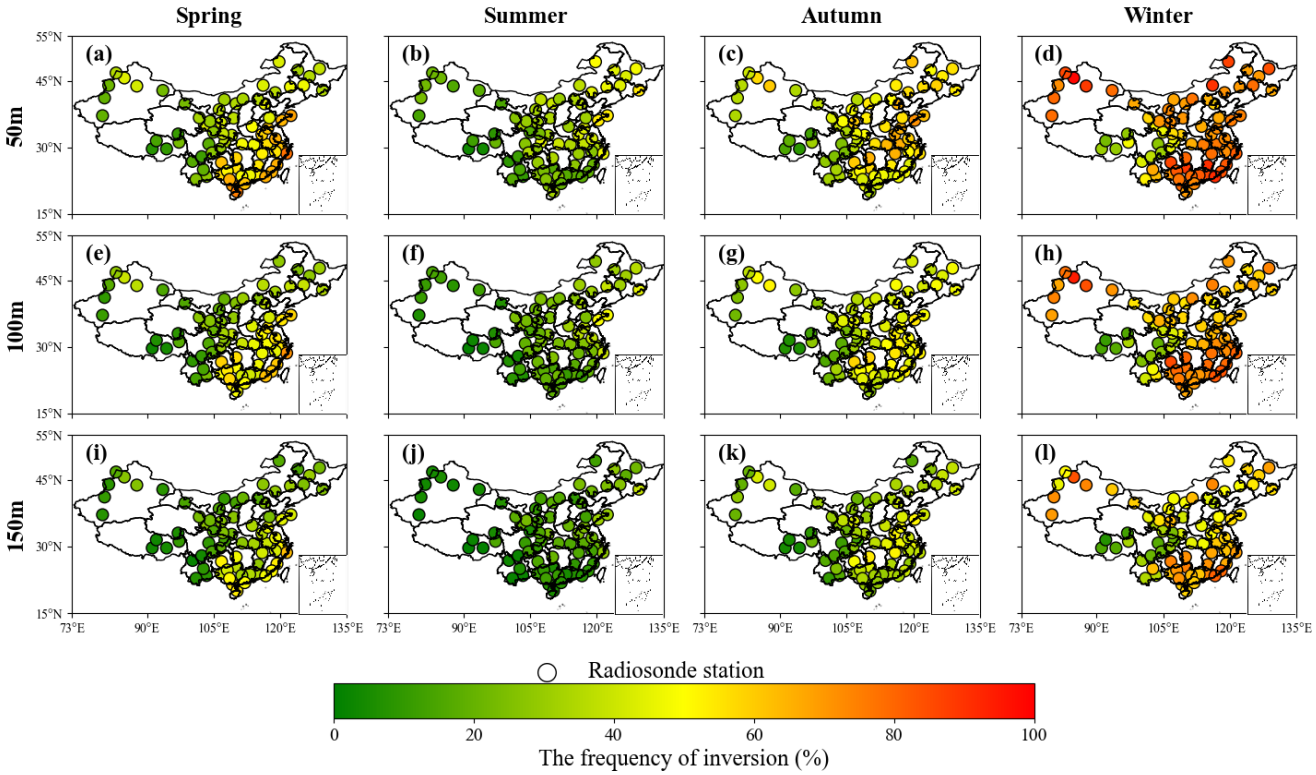

Fig S20. Distribution of EI frequency across different thickness thresholds.

S3. Case studies in BTH, YRD, and PRD.

To further investigate the dynamic relationship between temperature inversions (TIs) and pollution episodes across diverse climatic and emission regimes, we selected three representative cities for detailed analysis: Beijing (BTH), Nanjing (YRD), and Yangjiang (PRD) (Fig. S21). The analysis reveals distinct regional response patterns. In Beijing (Fig. S21a) and Nanjing (Fig. S21b), a clear "accumulation-persistence" process is observed. The intensification of TI acts as a physical trigger, followed by a progressive, lagged rise in $PM_{2.5}$ concentrations. Due to the high local emission loads in these regions, the pollution often persists even during periods of TI fluctuation, illustrating the sustained "lid effect" of atmospheric stability. In contrast, Yangjiang (Fig. S21c) demonstrates a more synchronized "immediate response" pattern, where $PM_{2.5}$ concentrations track TI strength closely. This high sensitivity suggests that in the PRD region, where background pollution is lower, air quality is more instantaneously modulated by changes in vertical dispersion capacity. Overall, these case studies confirm that while TIs are a primary driver of pollution accumulation, the specific temporal lag and magnitude of the pollution response are modulated by regional emission intensities.

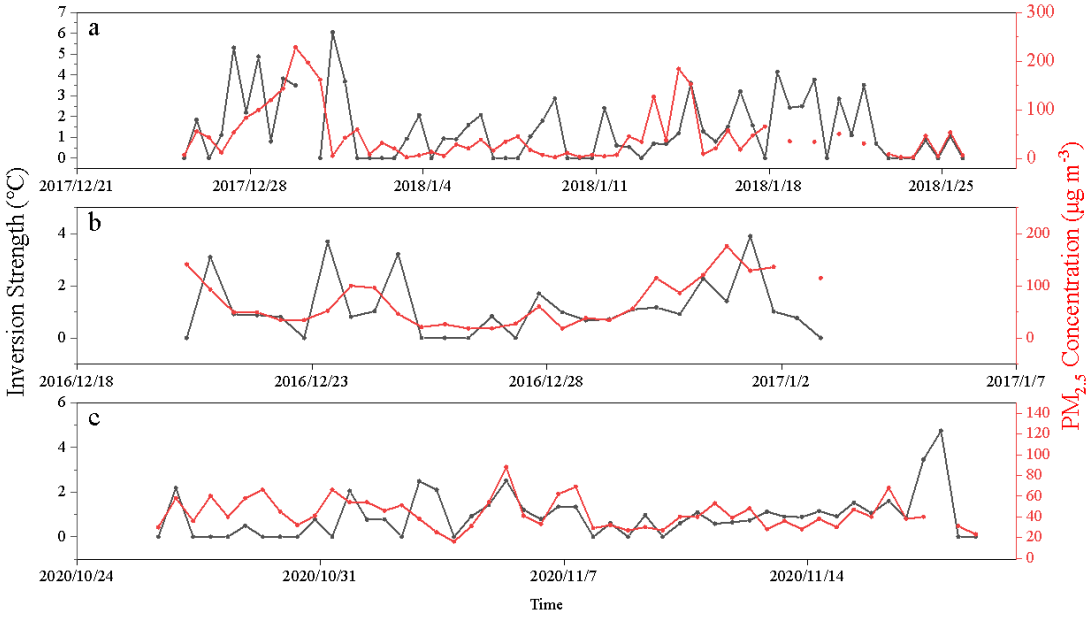

Fig S21. Temporal variations of temperature inversion (TI) strength and surface $PM_{2.5}$ concentrations during severe pollution episodes in representative cities. (a) Beijing (BTH region), (b) Nanjing (YRD region), and (c) Yangjiang (PRD region). The black line represents TI strength (ΔT, left axis), and the red line represents $PM_{2.5}$ concentration (right axis).

S4. Analysis of the "Inversion-Dispersion" Paradox in South China.

Combined PSCF and wind field analyses reveal that the air quality patterns in South China are driven by a 'Ventilation vs. Stagnation' mechanism (Fig. S22). Our data from Wuhan and Guangzhou confirm that while pollutants are indeed transported from the north, the EI periods in South China are often synchronized with strong northerly momentum. These winds act as a 'sweeper,' accelerating the southward dispersion of $PM_{2.5}$ into the sea and lowering local concentrations. Conversely, non-EI periods often coincide with weak southerly flow and topographic blocking by the Nanling Mountains, creating a semi-enclosed stagnation zone that facilitates local accumulation.

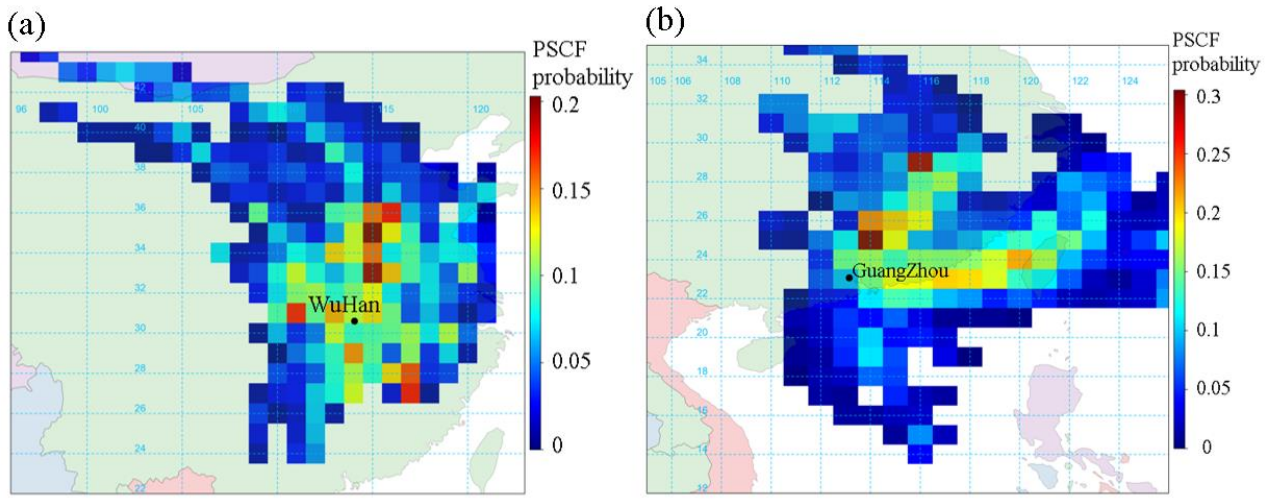

Figure S22. Spatial distribution of the Potential Source Contribution Function (PSCF) values for $PM_{2.5}$ during the study period. The analysis is based on 48-h backward trajectories at an altitude of 500 m. (a) Wuhan (representative of Central China), showing dominant potential sources from the North China Plain. (b) Guangzhou (representative of South China), indicating potential transport pathways primarily from Central China and the eastern coast.

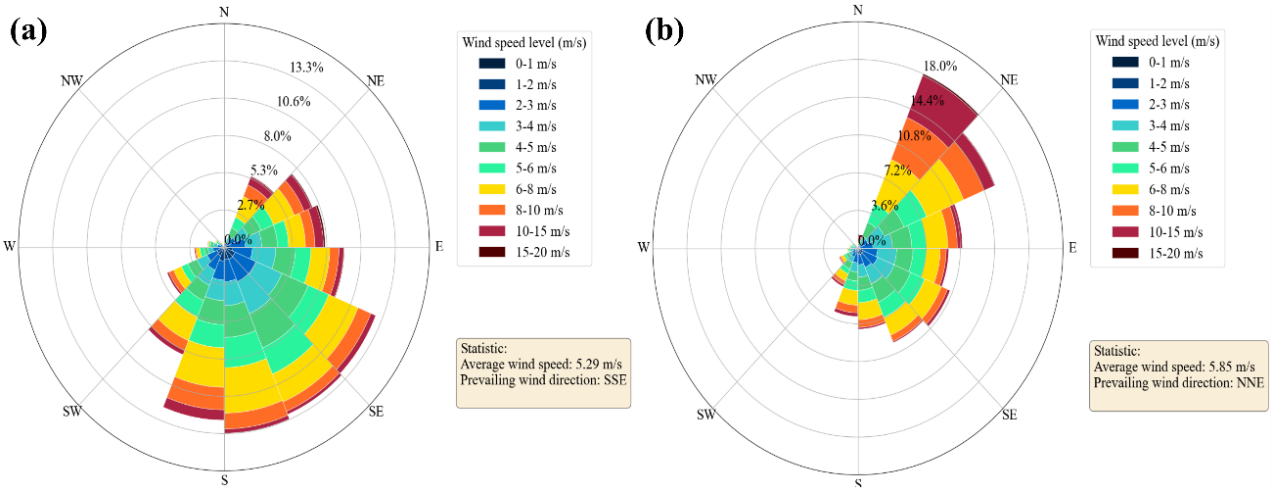

Figure S23. Roses of the mean boundary-layer wind (0–1000 m) in SC. (a) Patterns during non-inversion periods. (b) Patterns during the presence of EIs. Note that EIs are typically associated with stronger northerly winds (ventilation), while non-inversion periods are dominated by weaker southerly winds.